

Current- and Varifold-Based Registration of Lung Vessel and Airway Trees

Yue Pan, Gary E. Christensen, Oguz C. Durumeric, Sarah E. Gerard, Joseph M. Reinhardt
The University of Iowa, IA 52242

{yue-pan-1, gary-christensen, oguz-durumeric, sarah-gerard, joe-reinhardt}@uiowa.edu

Geoffrey D. Hugo
Virginia Commonwealth University, Richmond, VA 23298
geoffrey.hugo@vcuhealth.org

Abstract

Registering lung CT images is an important problem for many applications including tracking lung motion over the breathing cycle, tracking anatomical and function changes over time, and detecting abnormal mechanical properties of the lung. This paper compares and contrasts current- and varifold-based diffeomorphic image registration approaches for registering tree-like structures of the lung. In these approaches, curve-like structures in the lung—for example, the skeletons of vessels and airways segmentation—are represented by currents or varifolds in the dual space of a Reproducing Kernel Hilbert Space (RKHS). Current and varifold representations are discretized and are parameterized via of a collection of momenta. A momenta corresponds to a line segment via the coordinates of the center of the line segment and the tangent direction of the line segment at the center. A varifold-based registration approach is similar to currents except that two varifold representations are aligned independent of the tangent vector orientation. An advantage of varifolds over currents is that the orientation of the tangent vectors can be difficult to determine especially when the vessel and airway trees are not connected. In this paper, we examine the image registration sensitivity and accuracy of current- and varifold-based registration as a function of the number and location of momentum used to represent tree like-structures in the lung. The registrations presented in this paper were generated using the Deformetrica software package ([Durrleman et al. 2014]).

Keywords: *Diffeomorphic image registration, currents, varifolds, momenta, Reproducing Kernel Hilbert Space (RKHS)*

1. Introduction

Registration of lung CT images is important for many radiation oncology applications including assessing and adapting to anatomical changes, accumulating radiation dose for planning or assessment, and managing respiratory motion. For example, variation in the anatomy during radiotherapy introduces uncertainty between the planned and delivered radiation dose and may impact the appropriateness of the originally-designed treatment plan. Frequent imaging during radiotherapy accompanied by accurate longitudinal image registration facilitates measurement of such variation and its effect on the treatment plan. The cumulative dose to the target and normal tissue can be assessed by mapping delivered dose to a common reference anatomy and comparing to the prescribed dose. The treatment plan can then be adapted periodically during therapy to help mitigate the impact of these changes by ensuring the cumulative delivered dose is concordant with the prescribed dose [13, 9, 15]. Furthermore, image registration can also help measure how the tumor changes during or after treatment, which can potentially assist in predicting early response to therapy. These applications all rely on accurate tracking of lung motion over the breathing cycle and anatomical and functional changes over time.

Accurate image registration is critical for clinical implementation of these strategies. However, the ability of an algorithm to match anatomy throughout the lung may be limited by the complex variations in the anatomy and limited image contrast. One approach to improving registration accuracy is to highlight and extract known anatomy such as pulmonary airways or blood vessels [2] to improve the matching at these tissue locations.

Image registration correspondence can be defined either through intensity-based or feature-based approaches. Intensity-based approaches register images by minimizing differences in intensities between the moving (deformed template) and target images. In general, intensity-based

registration approaches have the advantage of not needing user intervention but often do a poor job of aligning features such as points, lines and surfaces contained in the images. Feature-based approaches are attractive because they directly match features, but they often require *a priori* point-to-point correspondence, which can be challenging in radiotherapy applications where this is often not known. Current- and varifold-based image registration are feature-based registration approaches with the advantage that no point correspondence is assumed between the objects being registered ([14],[5],[6]). The currents framework has been successfully applied to perform registrations of MR images ([14],[4],[5]) and also lung CT images ([8]). A varifold-based registration approach [3] is similar to current-based registration approach except that two varifold representations can be aligned in an orientation invariant manner which will be discussed in the next section.

Current- and varifold-based image registration is built using the Large Deformation Diffeomorphic Metric Mapping (LDDMM) framework ([11],[12]). This framework produces correspondence maps (transformations) between images that are guaranteed to be diffeomorphisms.¹ In this work, the velocity field of the LDDMM framework is represented by currents ([4]) and the control points of the deformation field are not necessarily dense in order to get desired registration results ([5],[7]). The results presented in this paper were generated using the Defometrica software ([Durrleman et al. 2014]), which is publicly available at www.defometrica.org. The contribution of this paper is a sensitivity analysis of the current- and varifold-based image registration methods to the number and location of momenta representing tree-like structures in the lung such as the centerline of the pulmonary vessel and airway trees.

2. Methods

Currents and varifolds are mathematical objects that can be used to model general geometrical objects. A current is a linear functional on a smooth manifold which is continuous in the sense of distributions. Any set of curves or surfaces can be represented in terms of currents. The advantage of using currents to register images is that the similarity measure is defined in the space of currents, which does not assume any kind of point-correspondence between structures. A varifold can be considered a generalization of the idea of a current in the sense that the tangent vector of its representative momenta are not oriented. Theoretically, varifolds are weaker objects than currents due to the lack of orientation of the tangent vector of the momenta used to represent a shape. However, this “weaker” side of varifolds is a desirable property when matching line segments with uncertain tangent orientation.

¹A diffeomorphism is a bijective, differentiable map between two manifolds such that its inverse is also differentiable.

2.1. Current Representation

The current representation of a curve L is defined by the path/line integral along the curve through a test vector field ω via

$$L(\omega) = \int_L \omega(x)^t \tau(x) d\lambda(x) \quad (1)$$

where, τ is the tangent of the curve at point x and $d\lambda$ is the Lebesgue measure on the curve. The test vector field ω is an element of a space of possible vector fields W , where W is a Reproducing Kernel Hilbert Space (RKHS). In this work, W is a space of square integrable vector fields convolved with a smoothing Gaussian kernel: $\omega(x) = K^W(x, \cdot)\alpha$, where the pair (x, α) is called a momentum. The tangent vector along the curve gives a natural action of the curve on vector fields. The norm of the current is defined in the dual space (currents space) W^* of W , as the maximum action of the current among all possible test vector fields. W is a closed span of the vector fields $\omega(x) = K^W(x, \cdot)\alpha$. The dual space of W denoted as W^* is a closed span of Dirac delta currents δ_x^α , where a Dirac delta current is the dual representation of the basis vector field $K^W(x, \cdot)\alpha$. Based on the Riesz representation theorem, there is a linear mapping between W and its dual space W^* , $\mathcal{L}_W : W \rightarrow W^*$ such that

$$\mathcal{L}_W(\omega)(\omega') = \langle \omega, \omega' \rangle_W \quad (2)$$

Therefore, $\delta_x^\alpha = \mathcal{L}_W(K^W(x, \cdot)\alpha)$

In a discrete setting, curves may be represented as polygonal lines where the direction of the tangent is constant over each line segment. In this case, the current representation of a polygonal curve is given by

$$L(\omega) = \sum_k \omega(x_k)^t \tau(x_k) \quad (3)$$

where x_k is the center of each line segment and $\tau(x_k)$ is the tangent vector at x_k . The magnitude of $\tau(x_k)$ is proportional to the length of the line segment centered at x_k .

2.2. Varifold Representation

A varifold is a generalization of a current in the sense that the tangent vector of its representative momenta are not oriented. A varifold representation provides an advantage over a current representation for representing structures in which the orientation of the constitute line segments are unknown or difficult to discern. This is true for the current application in which the vessel trees may consist of disconnected line segments due to, for example, where a tumor or other pathology interrupts the vessel trees.

The varifold representation of a curve L is defined by the path/line integral along the curve through a test vector field ω via

$$L(\omega) = \int_L \omega(x)^t \frac{\tau(x)^2}{\|\tau(x)\|} d\lambda(x) \quad (4)$$

where, τ is the tangent of the curve at point x and $d\lambda$ is the Lebesgue measure on the curve. The test vector field ω is an element of a space of possible vector fields W , where W is a RKHS. Notice that Equations 1 and 4 are nearly identical except for the term $\frac{\tau(x_k)}{\|\tau(x_k)\|}$ which always makes the orientation of the tangent vector positive in the varifold representation. The discrete version of Eq. 4 is given by

$$L(\omega) = \sum_k \omega(x_k)^t \frac{\tau(x_k)^2}{\|\tau(x_k)\|} \quad (5)$$

2.3. Diffeomorphic Deformation Framework

We first describe the image registration cost function for two curves represented by currents. Let L_1 and L_2 be two curves that we want to register. Each curve is mapped to its dual space currents representation denoted as T_1 and T_2 , respectively. Each current is represented as the finite sum of Dirac delta currents using Eq. 3 as $T_1 = \sum_n \delta_x^\alpha$ and $T_2 = \sum_m \delta_y^\beta$. The distance between two currents is defined as the norm squared difference of the currents computed in the RKHS dual space given by

$$\begin{aligned} \|T_1 - T_2\|_{W^*}^2 &= \left\| \sum_n \delta_x^\alpha - \sum_m \delta_y^\beta \right\|_{W^*}^2 \\ &= \sum_{n,n'} K^W(x_n, x_{n'}) \alpha_n^t \alpha_{n'} - 2 \sum_{n,m} K^W(x_n, y_m) \alpha_n^t \beta_m \\ &\quad + \sum_{m,m'} K^W(y_m, y_{m'}) \beta_m^t \beta_{m'} \end{aligned} \quad (6)$$

The image registration cost function for currents is defined as

$$C = \|\phi_* T_1 - T_2\|_{W^*}^2 + \gamma \left\| \sum_i v_{t_i}(x) \Delta \right\|_V^2 \quad (7)$$

where ϕ is the transformation from the coordinate system of current T_1 to that of T_2 and ϕ_* is the differential of ϕ . ϕ_* is also called the pushforward or total derivative of ϕ . The pushforward ϕ_* transforms the current T_1 into the coordinate system of the current T_2 . The second term in Eq. 7 is the discretized regularization term on the velocity of the transformation ϕ and is represented as $\int_0^1 \|v_t\|_V^2 dt$ in continuous setting. Δ is time interval. v_t is the velocity field at time t and can also be thought of as an element of a RKHS space. Therefore, it can be represented in terms of momenta

$$v_{t_i} = \sum_i K^V(\cdot, x_i(t)) \alpha_i(t) \quad (8)$$

where $(x_i(t), \alpha_i(t))$ is the time varying momenta that parameterizes diffeomorphic transformation model.

The image registration cost function for two curves represented by varifolds is similar to that for currents. Again, let L_1 and L_2 be two curves that we want to register. With

an abuse of notation, let $T_1 = \sum_n \delta_x^\alpha$ and $T_2 = \sum_m \delta_y^\beta$ be the Dirac delta varifold representation of L_1 and L_2 , respectively, using Eq. 5. With an additional abuse of notation for W^* , let the distance between two varifolds be defined as

$$\begin{aligned} \|T_1 - T_2\|_{W^*}^2 &= \sum_{n,n'} K^W(x_n, x_{n'}) \alpha_n^t \alpha_{n'} \\ &\quad - 2 \sum_{n,m} K^W(x_n, y_m) \frac{(\alpha_n^t \beta_m)^2}{|\alpha_n| |\beta_m|} \\ &\quad + \sum_{m,m'} K^W(y_m, y_{m'}) \beta_m^t \beta_{m'} \end{aligned} \quad (9)$$

The image registration cost function for varifolds is defined as

$$C = \|\phi_* T_1 - T_2\|_{W^*}^2 + \gamma \left\| \sum_i v_{t_i}(x) \Delta \right\|_V^2 \quad (10)$$

which appears similar to Eq. 7 except that T_1 and T_2 are the varifold representations of L_1 and L_2 , respectively, and W^* is the dual space of the varifold RKHS with our abuse of notation.

Momenta are used to parametrize the velocity field v_t of the transformation ϕ in a similar way that momenta are used to parameterize the shapes of the objects, T_1 and T_2 , to be registered. The relationship between the transformation ϕ and the time varying velocity field v_t is given by the O.D.E.

$$\frac{d}{dt} \phi_t^v(x) = v_t(\phi_t^v(x, t)) \quad (11)$$

where $t \in [0, 1]$ and $\phi = \phi_1^v$. The time varying transformation ϕ_t^v is a homotopy between the identity transformation at time $t = 0$ (i.e., $\phi_0^v = Id$) and the transformation ϕ that maps T_1 into the shape of T_2 at time $t = 1$ (i.e., $\phi_1^v = \phi$). The superscript v on the transformation ϕ_t^v denotes the dependence of the transformation on the velocity field v_t . Note that varifolds cannot be used to represent the velocity field since the velocity field is a vector field in which the direction of the vectors are important. In the case of parameterizing the velocity field with momenta, the magnitude of the vector no longer represents the length of a segment, but rather, it represents the velocity of the transformation at certain point in time. The momenta representing the velocity field can be considered as vector weighted control points of the velocity field. Note that the location of the momenta are not fixed during the registration process and are free to move around during the registration process. The Deformetrica software was used to find the optimal location and direction for the control points of the velocity field for registration for the results generated for this paper [7].

2.4. Extracting Vessel Tree Momenta from CT Images

For most radiation therapy interventions, the lung is imaged via CT. In a CT image, the vessels in a lung appear bright on a dark background. We used the Jerman et al. vesselness filter [10] to extract the vessel tree segmentation from a 3D CT image volume. In this method, the Hessian matrix is computed from the intensity values of the CT at each voxel location. Next, the eigenvalues are computed from the Hessian matrix. Tubular structures are then identified at voxel locations with one negligible eigenvalue and two similar non-zero negative eigenvalues. The vessel tree segmentations were then skeletonized using a morphological thinning algorithm in ITK (www.itk.org) to find the center line.

The vessel centerline detected as above resulted in a 26-neighbor connected set of discrete voxels. Connecting the centers of the skeletal voxel centers with line segments produces a piece-wise constant polygonal line with stair-step artifacts. A contour with stair-step artifacts gives a poor current and varifold representation since the tangent vectors from one line segment to the next do not vary smoothly. To overcome this problem, we fit a second order polynomial to each vessel branch using regression. We used the polyfit function in MATLAB (MathWorks, Natick, MA) to perform the regression. The fitted second order polynomial produced a smooth approximation to each branch that could be sampled at any resolution.

In this work, the momenta were sampled from the polynomial curves using units of pixels in 2D (voxels in 3D) in which the pixel (voxel) dimensions were isotropic. If branch length was not a multiple of the sampling period, we reduced the sample period enough to uniformly sample the branch.

2.5. Evaluation Methods

The registration results were evaluated using symmetric average closest distance between two shapes. The average closest distance from one shape consisting of multiple curves to another is computed by taking each point in one shape and finding the closest point on the second shape. These distances are then averaged to get the average closest point distance. The average closest distance measured from one shape to another is often different than the average closest point distance computed when the roles of the two shapes are reversed. To mitigate this problem, we compute the symmetric average closest point distance which is the average of the distance computed from shape I_1 to shape I_2 and the distance computed from shape I_2 to shape I_1 . The symmetric average closest point distance between two

shapes I_1 and I_2 is given by

$$d(I_1, I_2) = \frac{1}{2} \left(\frac{1}{N_1} \sum_{y \in I_1} \min_{x \in I_2} d(x, y) + \frac{1}{N_2} \sum_{x \in I_2} \min_{y \in I_1} d(y, x) \right). \quad (12)$$

2.6. Preprocessing

The Iterative Closest Point (ICP) [1] algorithm was used to rigidly align the shapes before registration. The main reason to use ICP is to remove the translational and rotational differences between the set of momenta locations of the moving and target shapes before nonrigid alignment.

3. Results

3.1. Sensitivity to the Number/Position of Momenta and the Kernel Size of the RKHS

There are the most important considerations for current and varifold registration of tree-like structures is (1) how to choose the number of the momenta, (2) how to choose the standard deviation λ_s of the Gaussian kernel K^W in Eq. 7 for the shape and (3) how to choose the standard deviation λ_ϕ of the Gaussian kernel K^V in Eq. 8 for the deformation field.

To start to answer these questions, we designed an experiment that registered eight pairs of simple 2D branch structures (see Fig. 1) multiple times using different numbers of momenta (see Fig. 2) and varying the shape kernel standard deviation λ_s . We kept the deformation kernel standard deviation λ_ϕ fixed at 250 for this experiment. The registration error was computed for each registration and was used to evaluate the performance of each registration.

Figure 1 shows four of eight pairs of structures that were registered in this experiment. In this figure, the blue shape was registered to the red shape. Note that the bottom point of the vertical line segment for all of the red and blue structures start at the same location. Registration pairs 5, 6, 7 and 8 are not shown in this figure since they reverse the roles of the fixed and moving structures shown in panels a, b, c and d, respectively. The shapes in this figure were chosen to mimic a single simple branching structure from a real 3D pulmonary airway or vessel tree.

Figure 2 shows how the momenta were positioned on one of the registration pairs. This figure shows that the momenta were uniformly spaced along each of the branches for a total of 3, 6, 9 and 12 momenta for each shape. The case of three total momenta corresponds to the limiting case of one momentum per branch. We limited this experiment to 4 momenta per branch since we wanted to determine the fewest number of momenta required to accurately represent a branch. The reason for this is that the computation time increases as the number of momenta increases.

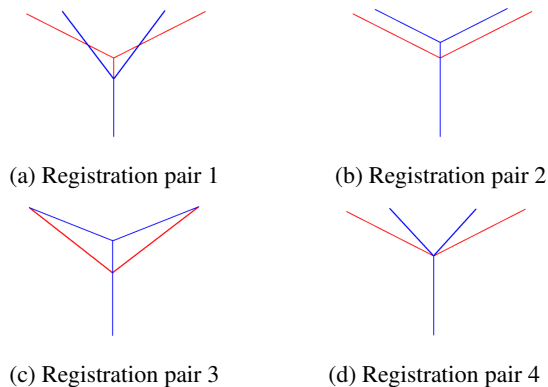


Figure 1: Simple 2D test structures used to characterize current- and varifold-based registration parameter selection. Red represents target structures and blue represents template structures. Registration pairs 5, 6, 7 and 8 are not shown in the figure; these registration pairs reverse the target and template structures shown in panels a, b, c and d, respectively. Note that the bottom point of the vertical line segment for all of the red and blue structures start at the same location.

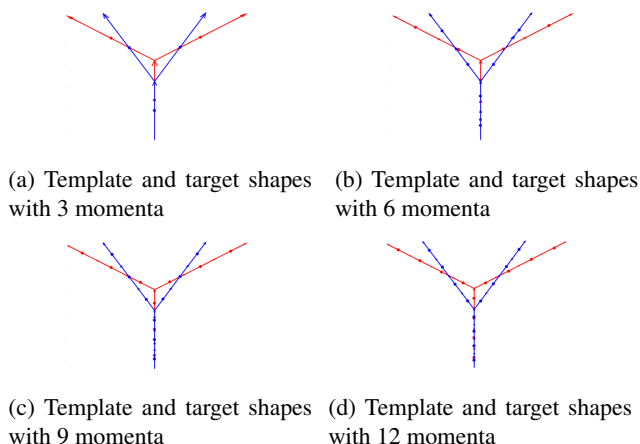


Figure 2: Examples showing the number and placement of momenta.

The graph in Fig. 3 shows the results of registering the eight pairs of branching shapes as a function of shape kernel standard deviation λ_s and the number of momenta used to parameterize the shape. Each curve on the graph corresponds to a different shape kernel standard deviation λ_s . Each point on a curve is the average value of all eight registration results.

The graph in Fig. 3 shows that for this experiment, the lowest registration error is achieved for the shape kernel size of $\lambda_s = 150/460 = 0.33$ and for nine momenta. The registration error is similar for 9 and 12 momenta, but we

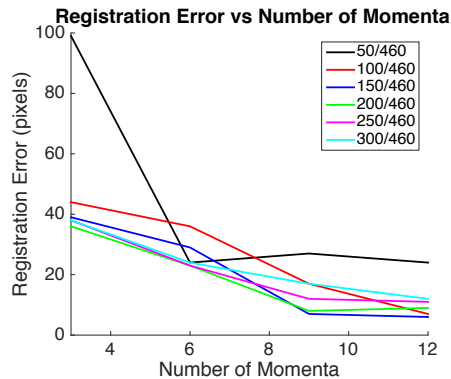


Figure 3: The effect of number of momenta on registration. For each kernel size, we use different number of momenta to represent the skeletons in the currents space and compute averaged registration error.

prefer the smaller of these two numbers.

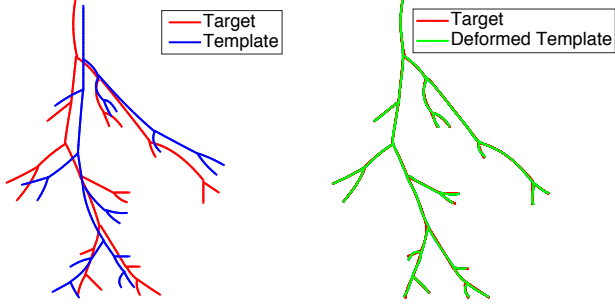
This experiment suggests that one should use three momenta per branch and a shape kernel size of 0.33 times the average branch length.

3.2. Vessel Tree Registration

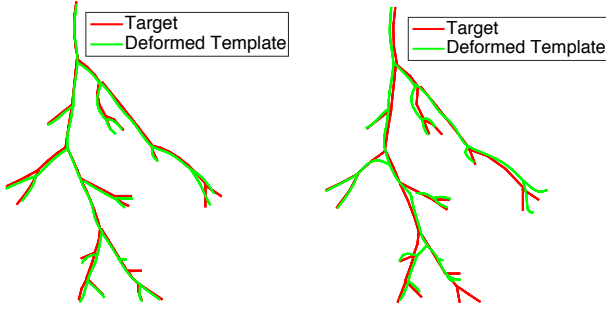
In the next series of experiments, we use two simple 2D vessel trees (see Fig. 4a) that were drawn to scale based on real 3D vessel trees extracted from CT images. The pixel dimensions for these vessel trees are 1 mm x 1 mm. In these experiments we varied the the deformation kernel standard deviation λ_ϕ , the shape kernel standard deviation λ_s and and the momenta sample period. The units for these variables are listed as pixels which are equal to 1 mm for these shapes.

Figure 4a shows two typical lung vessel branching structures with 31 branches and 15 branch points to be registered. The template (moving) vessel tree shape has 31 branches and 15 branch points. The minimum, maximum, mode and average (std dev) branch lengths were 7, 33, 9 and 13.1(6.18) pixels, respectively. The target vessel tree shape has 31 branches and 15 branch points. The minimum, maximum, mode and average (std dev) branch lengths were 6, 32, 8 and 13.8(6.48) pixels, respectively.

The vessel trees shown in 4a were registered $9 \times 3 \times 5 = 135$ times with 9 different momenta sampling periods, 4 different shape kernel standard deviations λ_s and 5 different deformation kernel standard deviations λ_ϕ . Panels 4b-4d show the registration results when the sampling period equaled 1, 5 and 9 pixels, respectively, while keeping the shape kernel standard deviation λ_s fixed at 3 pixels and the deformation kernel standard deviation λ_ϕ fixed at 10 pixels. Result shown in Panel 4b was the best registration result out of the 135 registrations. Figure 4 demonstrates that the reg-



(a) Template (moving) and target vessel trees before registration. Each vessel tree has 31 branches and 15 branch points. (b) Template and target shapes after registration: sample period = 1 pixel, deformation kernel size = 10 pixels, shape kernel size = 3 pixels.



(c) Template and target shapes after registration: sample period = 5 pixel, deformation kernel size = 10 pixels, shape kernel size = 3 pixels. (d) Template and target shapes after registration: sample period = 9 pixel, deformation kernel size = 10 pixels, shape kernel size = 3 pixels.

Figure 4: Examples showing the number and placement of momenta.

istration results got gradually worse as the sampling period increased.

Figure 5 shows the registration error as a function of the momenta sampling period and the shape kernel standard deviation λ_s . For these results the deformation kernel standard deviation λ_ϕ was fixed at 10 pixels. This figure shows that the best registration results were produced for the smallest sampling period.

Figures 6 and 7 shows the registration error as a function of the momenta sampling period and the deformation kernel standard deviation λ_ϕ . For these results the shape kernel standard deviation λ_s was fixed at 3 and 9 pixels, respectively. These figures show that the best registration results were produced for $\lambda_\phi = 10$ pixels which is roughly the same size as the mode of the template and target branch lengths.

Table. 1 shows that computation times increase as we decrease the deformation kernel size and decrease the momenta sampling period. The best registration results for

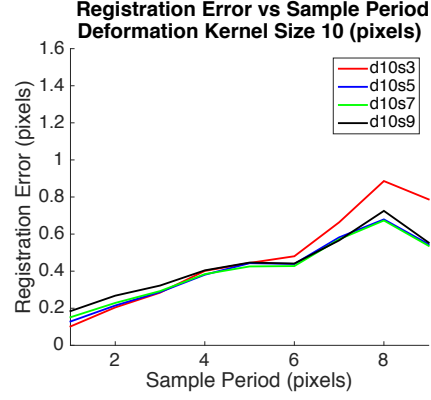


Figure 5: Registration error as a function of the momenta sampling period and the shape kernel standard deviation λ_s while keeping the deformation kernel standard deviation λ_ϕ was fixed at 10 pixels. The notation d10s3 corresponds to $\lambda_\phi = 10$ pixels and $\lambda_s = 3$ pixels.

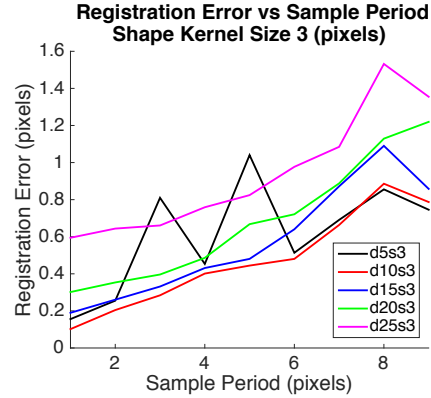


Figure 6: Registration error as a function of the momenta sampling period and the deformation kernel standard deviation λ_ϕ while keeping the shape kernel standard deviation λ_s was fixed at 3 pixels. The notation d10s3 corresponds to $\lambda_\phi = 10$ pixels and $\lambda_s = 3$ pixels.

the shapes shown in Fig. 4a were for sampling period 1 pixel, deformation kernel standard deviation 10 pixels and shape kernel standard deviation 3 pixels which took approximately 6 minutes to compute.

3.3. Varifold Orientation Robustness

Based on the definitions of currents (See Eq. 1) and varifolds (See Eq. 4), theoretically varifold representations should give better registration with unknown tangent orientations than currents. In order to learn more about the orientation robustness of the varifold representations, we did the following experiment. We use the same template and target

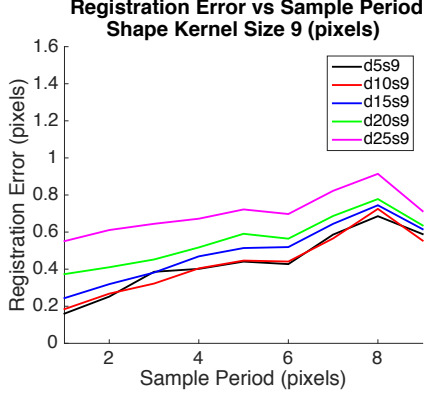


Figure 7: Registration error as a function of the momenta sampling period and the deformation kernel standard deviation λ_ϕ while keeping the shape kernel standard deviation λ_s was fixed at 9 pixels. The notation d10s3 corresponds to $\lambda_\phi = 10$ pixels and $\lambda_s = 3$ pixels.

Kernel Size	d5s3	d10s3	d15s3	d20s3	d25s3
SP = 1	30m 47s	6m 12s	2m 31s	1m 33s	1m 9s
SP = 5	43m 47s	3m 34s	1m 9s	27s	20s
SP = 9	38m 25s	3m 17s	40s	22s	17s

Table 1: Computation time with respect to different deformation kernel standard deviations λ_ϕ and momenta sample periods for the experiments shown in Fig. 4. SP represent the momenta sampling period in units of pixels. The notation d5s3 corresponds to $\lambda_\phi = 5$ pixels and $\lambda_s = 3$ pixels. For this registration experiment, the shape kernel standard deviation λ_s did not have a noticeable affect on the computation time. Note that the smaller the momenta sampling period, the more momenta were used to parameterize the template and target shapes. Note that the smaller λ_ϕ , the more momenta were needed to parameterize the registration transformation.

shapes as in Section 3.2. We manually flipped the orientation of some branches in our template shape (see Fig. 8) to see how the registration results of current- and varifold-representations differed. We sampled the template shape with sample period 1 and uses deformation kernel standard deviation $\lambda_\phi = 10$ pixels and a shape kernel standard deviation $\lambda_s = 3$ pixels.

First, we reversed the orientations of three branches on the template shapes and used currents and varifolds to represent our shape respectively.

The registration result of varifold representations is shown in Figure. 4b (a) and the registration result of current presentations is shown in Figure 8 (b). The region in

the black circles in Figure. 4b (a) and (b) shows the three branches where we flipped the orientations of tangent vectors. We can see inside the black circle, two shapes don't align well with current representations while the varifolds-based registration give as a better result.

Similarly, we flipped seven branches of the template shape as shown inside the black circle in 8 (c) and (d). We can see the registration result of current representations in 8 (c) is bad inside the black circle, while the registration result of varifold representation 8 (d) keeps the same.

Therefore, we can see varifolds representation is more robust to orientations of tangent vectors as we expected. As we showed in this experiment, when we flipped some branch's orientations, the registration result for varifold representations are the same no matter how many branches's orientations are flipped while the registration result of current presentations are not.

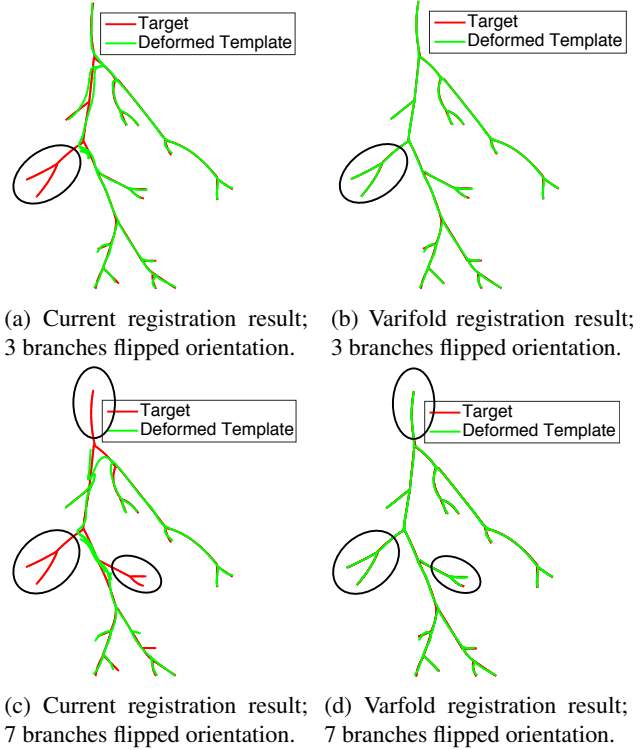


Figure 8: Registration results using current and varifold representations. The circles show the branches that had opposite tangent orientations between the template and the target. Notice that the current-based registration fails while the varifold-based registration does a good job of registering the shapes.

4. Discussion and Conclusions

This paper presented the mathematical framework for registering 3D pulmonary vessel and airway trees using cur-

rents and varifolds. We constructed 2D experiments using simple tree shapes to measure the sensitivity of current and varifold registration to (1) the momenta sample period Δ , (2) the standard deviation λ_s of the Reproducing Kernel Hilbert Space (RKHS) Gaussian kernel used to represent shapes and (3) the standard deviation λ_ϕ of the RKHS Gaussian kernel used to parameterize the diffeomorphic registration transformation. For the experiments presented, we conclude that the best registration results were produced when (1) Δ was as small as possible, (2) λ_ϕ was close to the mode of the template and target branch lengths and (3) λ_s was close to 1/3 of the mode of the template and target branch lengths. Note that the mode of the vessel tree branch lengths tends to be a measure of the average length of the branches near the leaf nodes of the tree. We showed that current- and varifold-based registration give equivalent results if the tangent orientations of the momenta are consistent between the moving shape and the target shape. We further showed that varifold-fold registration gives the same result for randomly oriented tangents.

5. Acknowledgements

This work was supported in part by the National Cancer Institute under award numbers R01CA166119 and R01CA166703. The content is solely the responsibility of the authors and does not necessarily represent the official views of the National Institutes of Health.

References

- [1] P. J. Besl and N. D. McKay. A method for registration of 3-D shapes. *IEEE Trans. Pattern Anal. and Machine Intelligence*, 14(2):239–256, 1992.
- [2] K. Cao, K. Ding, G. E. Christensen, M. L. Raghavan, R. E. Amelon, and J. M. Reinhardt. Unifying vascular information in intensity-based nonrigid lung ct registration. In *4th International Workshop on Biomedical Image Registration*, LCNS 6204, pages 1–12. Springer, July 2010.
- [3] N. Charon and A. Trouvé. The varifold representation of nonoriented shapes for diffeomorphic registration. *SIAM Journal on Imaging Sciences*, 6(4):2547–2580, 2013.
- [4] S. Durrleman. *Statistical models of currents for measuring the variability of anatomical curves, surfaces and their evolution*. PhD thesis, Université Nice Sophia Antipolis, 2010.
- [5] S. Durrleman, X. Pennec, A. Trouvé, and N. Ayache. Sparse approximation of currents for statistics on curves and surfaces. In *Medical Image Computing and Computer-Assisted Intervention—MICCAI 2008*, pages 390–398. Springer, 2008.
- [6] S. Durrleman, X. Pennec, A. Trouvé, P. Thompson, and N. Ayache. Inferring brain variability from diffeomorphic deformations of currents: an integrative approach. *Medical image analysis*, 12(5):626–637, 2008.
- [7] S. Durrleman, M. Prastawa, N. Charon, J. R. Korenberg, S. Joshi, G. Gerig, and A. Trouvé. Morphometry of anatomical shape complexes with dense deformations and sparse parameters. *NeuroImage*, 101:35–49, 2014.
- [8] V. Gorbunova, S. Durrleman, P. Lo, X. Pennec, and M. de Bruijne. Curve- and surface-based registration of lung ct images via currents. In *Second International Workshop on Pulmonary Image Analysis*, pages 15–25, 2009.
- [9] M. Guckenberger, J. Wilbert, A. Richter, K. Baier, and M. Flentje. Potential of adaptive radiotherapy to escalate the radiation dose in combined radiochemotherapy for locally advanced non-small cell lung cancer. *International Journal of Radiation Oncology* Biology* Physics*, 79(3):901–908, 2011.
- [10] T. Jerman, F. Pernuš, B. Likar, and Ž. Špiclin. Beyond frangi: an improved multiscale vesselness filter. In *SPIE Medical Imaging*, pages 94132A–94132A. International Society for Optics and Photonics, 2015.
- [11] R. McLachlan and S. Marsland. Discrete mechanics and optimal control for image registration. *Anziam Journal*, 48:1–16, 2007.
- [12] M. I. Miller, A. Trouvé, and L. Younes. Geodesic shooting for computational anatomy. *Journal of mathematical imaging and vision*, 24(2):209–228, 2006.
- [13] J.-J. Sonke and J. Belderbos. Adaptive radiotherapy for lung cancer. In *Seminars in radiation oncology*, volume 20, pages 94–106. Elsevier, 2010.
- [14] M. Vaillant and J. Glaunès. Surface matching via currents. In *Information Processing in Medical Imaging*, pages 381–392. Springer-Verlag, July 2005.
- [15] E. Weiss, S. P. Robertson, N. Mukhopadhyay, and G. D. Hugo. Tumor, lymph node, and lymph node-to-tumor displacements over a radiotherapy series: Analysis of interfraction and intrafraction variations using active breathing control (abc) in lung cancer. *International Journal of Radiation Oncology* Biology* Physics*, 82(4):e639–e645, 2012.